

1 Mapping Charge Recombination and the Effect of Point Defect Insertion in Gallium 2 Arsenide Nanowire Heterojunctions

3 Brian Zutter,¹ Hyunseok Kim,² William Hubbard,¹ Dingkun Ren,²
4 Matthew Mecklenburg,³ Diana Huffaker,^{2,4} and B. C. Regan^{1,*}

5 ¹*Department of Physics & Astronomy and California NanoSystems Institute,
6 University of California, Los Angeles, California 90095 USA*

7 ²*Department of Electrical Engineering, University of California, Los Angeles, California 90095 USA*

8 ³*Core Center of Excellence in Nano Imaging (CNI),*

9 *University of Southern California, Los Angeles, California, 90089 USA*

10 ⁴*School of Physics and Astronomy, Cardiff University, Cardiff CF24 3AA, United Kingdom*

11 (Dated: August 10, 2021)

12 Electronic devices are extremely sensitive to defects in their constituent semiconductors, but lo-
13 cating electronic point defects in bulk semiconductors has previously been impossible. Here we apply
14 scanning transmission electron microscopy (STEM) electron beam-induced current (EBIC) imaging
15 to map electronic defects in a GaAs nanowire Schottky diode. Imaging with a non-damaging 80 or
16 200 kV STEM acceleration potential reveals a minority-carrier diffusion length that decreases near
17 the surface of the hexagonal nanowire, thereby demonstrating that the device's charge collection
18 efficiency (CCE) is limited by surface defects. Imaging with a 300 keV STEM beam introduces
19 vacancy-interstitial (VI, or Frenkel) defects in the GaAs that increase carrier recombination and
20 reduce the CCE of the diode. We create, locate, and characterize a single insertion event, deter-
21 mining that a defect inserted 7 nm from the Schottky interface broadly reduces the CCE by 10%
22 across the entire nanowire device. Variable-energy STEM EBIC imaging thus allows both benign
23 mapping and pinpoint modification of a device's e-h recombination landscape, enabling controlled
24 experiments that illuminate the impact of both extended (1D and 2D) and point (0D) defects on
25 semiconductor device performance.

26 Crystal defects in semiconductor devices, whether 54 present at fabrication or introduced later via radiation 55 damage, can dramatically impair device performance[1– 56 6]. Commonly-used methods for characterizing semi- 57 conductor defects have spatial resolution that is crude 58 compared to the feature size in modern microelectronic 59 devices. For example, capacitance-voltage (CV) profil- 60 ing [7] and deep-level transient spectroscopy (DLTS)[8] 61 can extract defect concentrations and energy levels, re- 62 spectively, from simple heterojunctions. But the spatial 63 information provided by these techniques is one dimen- 64 sional at best. Two dimensional mapping is possible with 65 scanning electron microscope electron-beam induced cur- 66 rent (SEM EBIC) imaging, which can locate electrically- 67 active extended (i.e. one- and two-dimensional) defects[3, 68 9–11], monitor the development of conducting filaments 69 in metal-oxide resistive memory[12], measure depletion 70 region widths [13], and map minority carrier diffusion 71 lengths[3, 14–16]. However, the spatial resolution of SEM 72 EBIC imaging is limited by the size of its e-h (electron- 73 hole) generation volume[17]. In a standard, electron- 74 opaque SEM sample, most primary (beam) electrons de- 75 posit nearly all of their energy in the sample. The re- 76 sulting pear-shaped e-h generation volumes are of order 77 100 nm on a side[17, 18], which is large compared to fea- 78 ture sizes in many modern devices.

79 Because a STEM sample is electron-transparent, the
80 corresponding e-h generation volume is the cylindrical,

54 narrow neck of the SEM e-h generation pear[19]. With
55 this much smaller e-h generation volume STEM EBIC
56 imaging has the potential to achieve much higher spatial
57 resolution than SEM EBIC imaging[20–26]. Moreover,
58 the higher beam energies accessible with STEM (usually
59 60–300 keV vs. the 1–30 keV of SEM) span the knock-
60 on threshold in semiconductors, which allows a STEM
61 operator to choose whether or not to introduce knock-
62 on displacements in a semiconductor device *precisely* at
63 the position of the sub-nm² STEM beam. The combi-
64 nation of superior spatial resolution and precision mod-
65 ification enables *in situ* STEM EBIC experiments that
66 directly reveal e-h recombination physics in semicon-
67 ductor nanodevices. In essence, the STEM's focused elec-
68 tron beam serves both as a highly localized source of
69 β -radiation damage, and as an immediate local probe
70 of its effects. This combination allows individual point
71 (i.e. zero-dimensional) defects to be located to within
72 $< 1 \text{ nm}^2$.

73 To produce targets for demonstrating these capa-
74 bilities, we fabricate heterojunctions in semiconductor
75 nanowires (Fig. 1a), which are model systems for elu-
76 cidating defect physics[5, 14–16, 27–29]. We put Au
77 contacts on 130 nm-diameter p-type GaAs nanowires
78 (Fig. S1) with electron-beam lithography, and then
79 briefly anneal the devices [30, 31] (see Supplementary
80 Information). At elevated temperatures gallium and ar-
81 senic interdiffuse with the gold at the contacts, forming
82 abrupt ($< 2 \text{ nm}$) axial Au-GaAs heterojunctions aligned
83 with the (111) GaAs planes (Fig. 1b). Since the growth
84 direction of the GaAs nanowires is along the [111] crys-

* regan@physics.ucla.edu

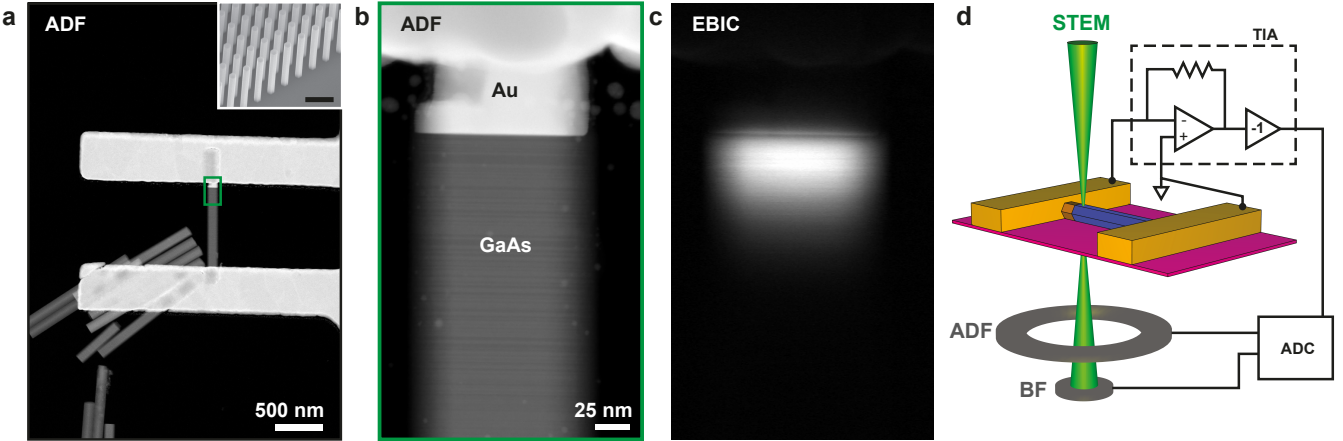


FIG. 1. **STEM EBIC imaging of a Au-GaAs nanowire heterojunction.** A low-magnification, 200 kV STEM annular dark-field (ADF) image (a) of a device shows 130 nm diameter GaAs nanowires and 250 nm-thick, lithographically-defined gold contacts supported by a 15 nm-thick silicon nitride membrane. An SEM image (a, inset) acquired with 30° stage tilt, shows the nanowires as grown, before transfer to the silicon nitride membrane (unlabeled scale bar is 500 nm). When the region indicated in green in (a) is imaged at higher-magnification (b), twin boundaries in the GaAs appear as horizontal lines separated by a few nm (Figs. 5a–e show such boundaries more clearly in another device). An EBIC image (c), acquired simultaneously with (b), reveals the e-h separation that occurs near the Au-GaAs heterojunction. The electrical connections and the locations of the TIA, STEM detectors (ADF,BF), and analog-to-digital converter (ADC) are indicated on a cartoon (d).

1 talline direction, these heterojunctions are self-aligned 33
2 perpendicular to the nanowire axis. Striations in STEM 34
3 annular dark-field (ADF) images of the GaAs nanowire 35
4 (Fig. 1b) indicate twin boundaries within the zincblende 36
5 crystal[27]. 37

6 Connecting a transimpedance amplifier to a device 38
7 (Fig. 1) allows us to generate a STEM EBIC image simul- 39
8 taneously with every STEM ADF image [20, 24, 25]. The 40
9 contrast mechanisms generating the two types of images 41
10 are entirely different, and thus the images provide com- 42
11plementary information. The ADF images (Fig. 1a,b) 43
12 provide information only about the device's physical 44
13 structure (e.g. composition and crystal lattice orienta- 45
14 tion), while the EBIC image (Fig. 1c) also reveals the 46
15 device's electronic structure, in this case the CCE, the 47
16 size of the space-charge region, and the minority carrier 48
17 diffusion length. 49

18 We understand the EBIC signal as being generated as 50
19 follows. Within some generation volume G surrounding 51
20 the path of the primary electrons through the sample, 52
21 the STEM electron beam creates e-h pairs. The pairs are 53
22 created by plasmon decay or by secondary electrons re- 54
23 sulting from primary electrons [18, 19]. The electron-hole 55
24 pairs then diffuse some distance, parametrized by a diffu- 56
25 sion length L , before recombining probabilistically with 57
26 a hole. Electrons that happen to diffuse to the space- 58
27 charge region near the Au-GaAs heterojunction can be 59
28 permanently separated from their holes by the built-in 60
29 electric field E . The separated charge is collected by the 61
30 electrodes and constitutes the EBIC. The CCE, which 62
31 here is the ratio of the EBIC to the rate of e-h pair gen- 63
32 eration, determines what fraction of e-h pairs are col- 64

lected. The e-h generation rate is relatively insensitive to crystal defects, while the CCE is lowered by recombination centers within the GaAs. Thus relative changes in CCE due to carrier recombination have a proportional effect on the EBIC. The EBIC also depends on the beam position within the nanowire through three size scales: the radius R of the e-h generation volume, the diffusion length L , and the thickness t of the space-charge region (i.e. the region with non-zero E). A single EBIC image can provide information on each of them[32].

51 Imaging another device with STEM ADF (Fig. 2a) and 52 STEM EBIC (Fig. 2b) shows how these length scales 53 collectively determine the shape of the EBIC profile 54 (Fig. 2c). The STEM ADF image shows the location 55 of the heterojunction, twin boundaries in the GaAs, and 56 some voiding in the Au. The STEM EBIC image shows 57 a CCE that varies in a non-trivial way as a function of 58 position. Just as the point-spread function limits the 59 resolution of e-beam lithography[33], the size of the e-h 60 generation volume, G , limits the EBIC electronic spatial 61 resolution. It manifests itself clearly here in at least two 62 ways [34]. First, a non-zero EBIC is generated when the 63 beam is incident on the Au side of the heterojunction, 64 even though e-h pairs are not separated in the Au bulk. 65 Fitting an EBIC line profile along the nanowire centerline 66 on the Au side of the heterojunction (Fig. 2c, blue 67 profile, purple line) to an exponential $I \propto e^{x/R_{Au}}$ yields a 68 decay length $R_{Au} = 9.4 \pm 0.2$ nm, where the error bar 69 reflects the statistical uncertainty in a linear least-squares 70 fit. This length scale R_{Au} measures how far from the 71 heterojunction the beam can be and still create e-h pairs 72 that get separated. (While labeled as the radius R of

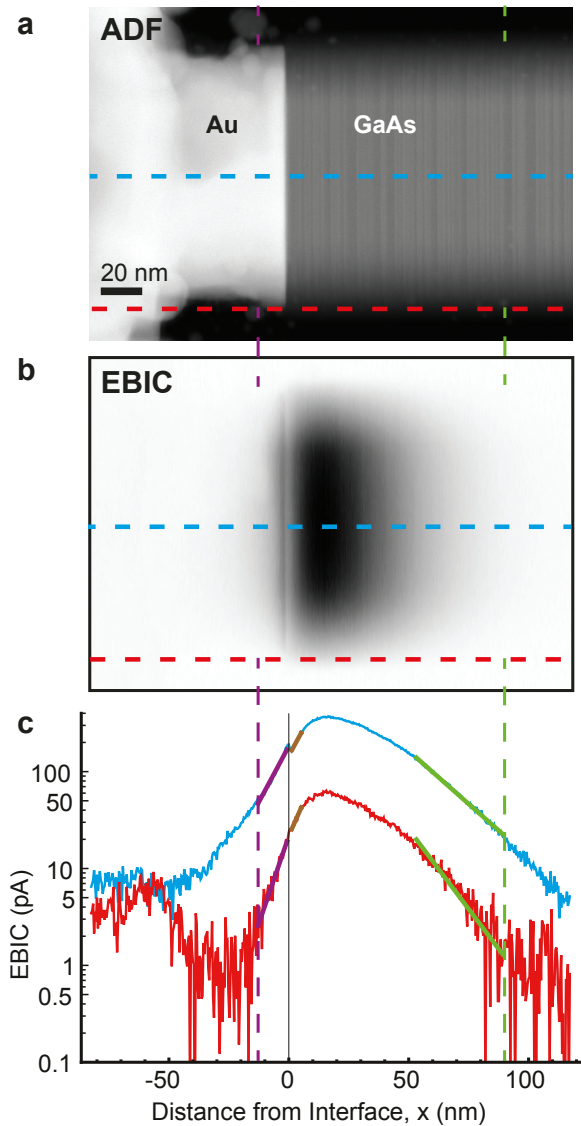


FIG. 2. **Mapping e-h recombination along the nanowire.** A STEM ADF image (a) and EBIC image (b) are acquired simultaneously with a 200 kV accelerating potential. EBIC line profiles (c) are extracted from the center (dashed blue line) and the edge (dashed red line) of the device in (a,b). The EBIC decay length in the Au (purple line) and the GaAs (brown line) measures the radius R of the e-h generation volume G in each material. In the GaAs far (> 50 nm) from the interface, the EBIC decay length (green line) measures the minority-carrier diffusion length L . All panels are aligned on the same x axis.

¹ G within the Au, this variable might be better labeled L_{Au} instead, depending on whether the EBIC is primarily generated by secondaries that produce e-h pairs in the GaAs, or by e-h pairs in the Au that diffuse to the heterojunction[35].) Second, the EBIC profile maximum 20 nm away from the heterojunction interface indicates that, when the beam is in the GaAs near the hetero-

junction, some of the G is in the Au, where the CCE is much smaller. Fitting an EBIC line profile along the nanowire center-line on the GaAs side of the heterojunction (Fig. 2c, blue profile, brown line) to an exponential $I \propto e^{x/R_{\text{GaAs}}}$ yields $R_{\text{GaAs}} = 9.6 \pm 0.4$ nm, which indicates the radius R of G within the GaAs. This model also explains the hiccup in the line profiles (also clearly visible in Fig. 2b) at the heterojunction: moving across the boundary into the Au actually increases the EBIC (even though e-h pairs are not separated in the Au bulk) because G is continuous while the absolute number of secondary electrons increases discontinuously.

On the Au side of the heterojunction the electric field $E = 0$, while on the GaAs side a substantial electric field $E \neq 0$ exists in the space-charge region. Thus near the heterojunction the CCE is a step function with approximate values of zero within the Au and unity within the GaAs [32], and the $\text{EBIC} \propto G \times \text{CCE}$ measures G as just described. Far (> 50 nm) from the heterojunction in the GaAs the E -field returns to zero, the minority-carrier transport is dominated by diffusion, and the EBIC measures the CCE. With increasing distance from the space charge region the EBIC in the GaAs decays exponentially, with a decay length equal to the minority-carrier diffusion length L . Fitting the EBIC current in the center of the nanowire (Fig. 2c, blue profile) to $I \propto e^{-x/L}$ [18], where x is the distance from the heterojunction, gives $L = 19.7 \pm 0.1$ nm (green line), where the error bar again reflects the statistical uncertainty in a linear least-squares fit. This relatively short diffusion length likely results not from the nanowire's dense zincblende twin boundaries (Fig 2a), but rather from surface recombination [15]. For instance, the surface-to-volume ratio at the thin edge of the nanowire is larger, and an EBIC profile at the edge (Fig. 2c, red profile) shows a much smaller minority-carrier diffusion length $L = 13.2 \pm 0.9$ nm (green line). Thus e-h pairs generated nearer the nanowire surface are more likely to recombine. While L is much smaller than the nanowire diameter $D = 130$ nm, this fact is not as surprising as it might seem at first: on average, any point in a long cylinder of diameter D is only a distance $D/6$ away from the cylinder surface.

The nanowire's simple shape facilitates the interpretation of the EBIC data. ADF STEM data (Fig. 3a = Fig. 2a rotated) show that the nanowire's cross-section (Fig. 3b) is a near-perfect hexagon (Fig. 3c). To give a sense of scale, a slice of a cylindrical e-h generation volume with $R = 10$ nm is superimposed on the GaAs nanowire's hexagonal cross section in Fig. 3c.

STEM EBIC imaging's extraordinary spatial resolution reveals how charge recombination varies as a function of not only the nanowire's axial coordinate, but also its radial coordinate (compare e.g. Ref. 15). Extending the STEM EBIC analysis of Fig. 2 by fitting at every distinct axial coordinate, we map both the minority-carrier diffusion lengths L (which determine the CCE) and the radii R (which determine G) across the width of the nanowire. The diffusion length L decreases from

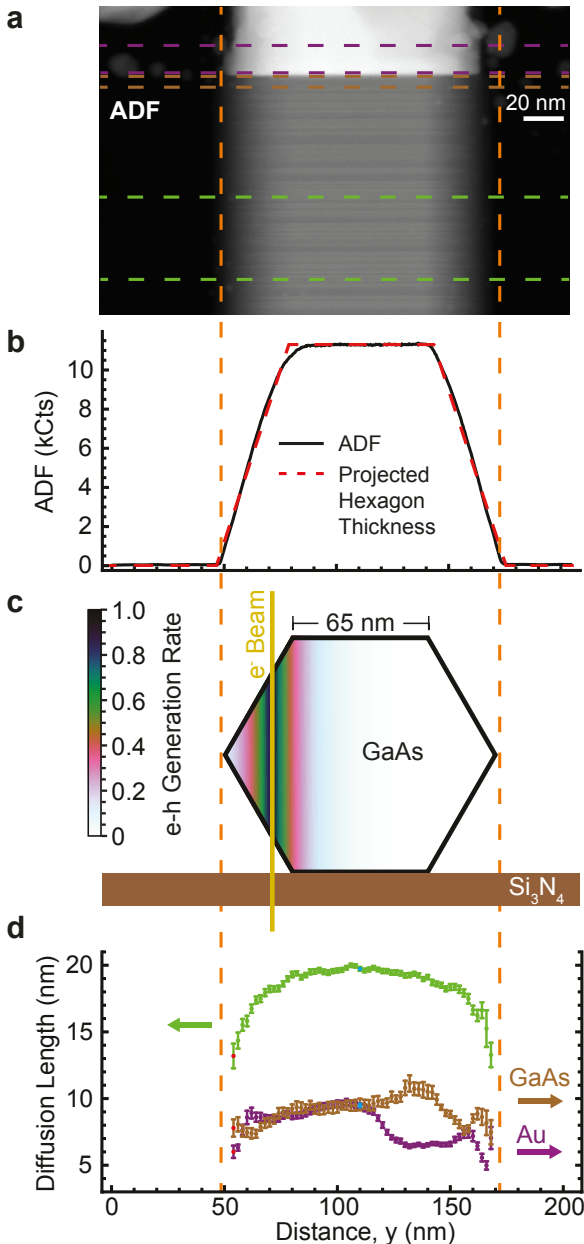


FIG. 3. Mapping e-h recombination across the nanowire. (a) The data of Fig. 2a are rotated 90° to align the Schottky interface with the horizontal axis. Summing the ADF signal from the dashed-green ROI in (a) gives a profile (b) approximately proportional to the sample thickness. This profile agrees well with the projected thickness of a geometrically-perfect hexagon (dashed-red line in b). A slice of the cylindrical e-h generation volume is overlaid on the nanowire cross-section (c), with a decay radius $R = 10$ nm. The generation volume radii R in Au and GaAs and the minority-carrier diffusion length L in the GaAs are plotted as a function of radial position across the hexagonal nanowire in (d). The L and R measurements shown explicitly in Fig. 2d are highlighted in blue (center) and red (edge) here. All panels are aligned horizontally on the same distance axis.

1 20 nm near the center axis of the 130 nm-wide nanowire
 2 to 13 nm near the edges (Fig. 3d, green plot), as expected
 3 for recombination occurring primarily at the nanowire
 4 surface.

5 The generation volume G 's effective radius R is less
 6 than 10 nm in both the Au (Fig. 3d, purple points)
 7 and the GaAs (brown points). Due to voiding in the
 8 Au (see Figs. 2a and 3a), these curves are irregular on
 9 one side of the nanowire. Near the nanowire's center
 10 the corresponding (cylindrical) STEM EBIC generation
 11 volume is $G \sim 4 \times 10^4$ nm³, while an SEM generation
 12 volume with effective radius $r \simeq 100$ nm (appropriate for
 13 a 5 keV accelerating voltage[17]) is $\times 100$ larger. STEM
 14 EBIC's resolution advantage is $\sim r/R$, or a factor of 10,
 15 relative to SEM EBIC.

16 Taking the 'electronic structure resolution' to be the
 17 full-width, half-maximum (FWHM) of the generation
 18 volume, our measured resolution is $(2 \ln 2)R = 14$ nm.
 19 Note that our STEM EBIC images show smaller features,
 20 implying better STEM EBIC resolution, but that these
 21 features are primarily generated by changes in physi-
 22 cal structure, not electronic structure. For instance, the
 23 STEM EBIC images show both the thickness variations
 24 that accompany the twin boundaries (~ 2 nm) and the
 25 EBIC hiccup (~ 3 nm) at the heterojunction (Fig. S6).

26 This resolution advantage creates qualitatively new ca-
 27 pabilities: STEM EBIC, unlike SEM EBIC, can map de-
 28 vice parameters like the minority-carrier diffusion length
 29 across an individual nanowire. Our measured R_{GaAs} of
 30 10 nm is an order-of-magnitude larger than predicted by
 31 the CASINO Monte Carlo simulator[19, 36, 37]. We at-
 32 tribute this discrepancy to CASINO's omission of plas-
 33 mon generation (the dominant energy loss mechanism in
 34 GaAs for electrons of < 50 eV energy [38]) in its calcu-
 35 lation of stopping power at low electron energies.

36 Within 50 nm of the interface, the EBIC signal is be-
 37 low the continuation of the green lines on the log-linear
 38 plot (Fig. 2c). Near the heterojunction we might instead
 39 expect the EBIC increase as the local E -field increases
 40 in the space-charge region. As mentioned above, the ob-
 41 served decrease indicates that some of the e-h generation
 42 volume G is in the Au (Fig. 3d). Based on the position of
 43 the knee in the EBIC data, the thickness t of the space-
 44 charge region is ~ 50 nm.

45 To compare damage rates at various accelerating volt-
 46 ages, we image the device of Figs. 2 and 3 while keep-
 47 ing all other imaging conditions (e.g. the 50 pA STEM
 48 beam current, 762 μ s pixel dwell time, and 0.87 nm pixel
 49 size) constant (Fig. 4). Repeated imaging at 80 kV and
 50 200 kV has little effect on the EBIC, but 300 kV imag-
 51 ing markedly reduces the EBIC signal (Fig. 4a). (The
 52 EBIC magnitude decreases as the accelerating potential
 53 increases because higher energy electrons deposit less en-
 54 ergy per distance traveled in a solid [39].)

55 As a function of dose, the EBIC, and thus the CCE,
 56 decreases linearly at 300 kV (Fig. 4b). We attribute
 57 the reduction in CCE to knock-on damage that intro-
 58 duces electronically-active vacancy-interstitial (VI) de-

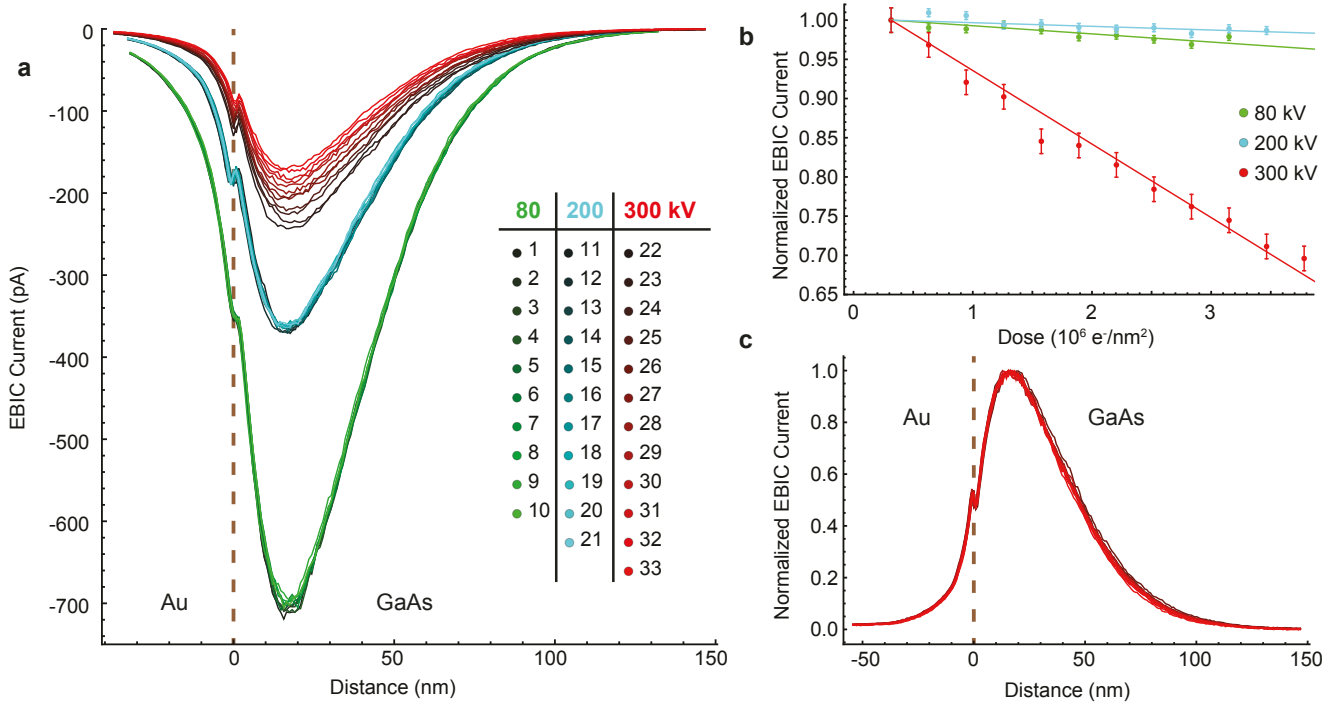


FIG. 4. STEM EBIC at 80, 200, and 300 kV accelerating voltage. Line profiles (a) show the effect of repeated imaging of a device (shown in Fig. 5) at 80 kV (green), 200 kV (cyan) and 300 kV (red). Line profiles are extracted from the cyan boxes shown in Fig. 5a. Only the 300 kV curves show a significant decrease in the EBIC with repeated imaging. Plotting the profile minima, normalized relative to their initial values, versus dose shows (b) a linear dose effect at 300 kV and insignificant effects at 80 and 200 kV. At 300 kV the maximum EBIC decreases by $\sim 3\%$ per image. Error bars on the 80, 200 and 300 kV data series are determined by setting the reduced $\chi^2 = 1$ for the linear fits. Normalizing the profiles of the 300 kV data series by the minimum value of each (c) shows that only the amplitude of the EBIC line profile changes, not the shape.

1 effects, probably on the As sublattice [40]. These defects 26 function as e-h recombination centers, reducing the cur- 27 rent that is collected to form the EBIC signal. Energy 28 and momentum conservation dictate that the maximum 29 possible energy transfer from a beam electron to a gal- 30 lium (mass number $A = 70$) nucleus is 2.7, 7.5, and 31 12.2 eV for incident electron kinetic energies of 80, 200, 32 and 300 keV, respectively [39]. The maximum energy 33 transfer varies inversely with the mass of the target nu- 34 cleus, so the numbers for arsenic ($A=75$) are nearly the 35 same (2.5, 7.0, and 11.4 eV, respectively). Gold ($A=197$) 36 allows only $70/197 \sim 1/3$ the energy transfer, which 37 is small enough at all of the accelerating voltages used 38 in these experiments that the displacement or knock-on 39 damage in this material is negligible. But the displace- 40 ment damage threshold energy in GaAs is ~ 10 eV [1, 40– 41 42] (although with substantial uncertainty — see Ref. [42] 42 and references within), which leads us to expect an onset 43 of electron beam-induced displacement damage between 44 the accelerating voltages of 200 and 300 kV. 45

21 One might expect sputtering to be a more important 46 damage mechanism than displacement, since sputtering 47 has larger cross sections and smaller threshold energies 48 [43]. However, while we expect that sputtering does oc- 49 cur in these experiments, we do not attribute the CCE 50

drop to this mechanism for two reasons. First, sputtering is expected at all three accelerating voltages, but changes in EBIC are insignificant at 80 and 200 kV (Fig. 4). Second, the EBIC spatial profile is consistent with a surface recombination probability near unity (Figs. 2–3). In short, while sputtering damage doubtless occurs, the nanowire surface is already so defective that further damage has no significant effect on the e-h recombination probability.

After they have been normalized relative to their minima, all twelve EBIC profiles acquired at the damaging 300 kV accelerating voltage overlap closely (Fig. 4c). That the defects introduced do not change the minority-carrier diffusion length L indicates that L is still dominated by surface recombination, and that this length scale is determined by the nanowire cross section as discussed earlier.

Repeated imaging of this device at 300 kV thus causes a substantial reduction in the EBIC (and thus the CCE) of the nanowire junction — the radiation damage destroys this device’s ability to effectively separate of e-h pairs. Given the large dose (six million 300 keV electrons per square nanometer) and accompanying efficiency drop, it is remarkable that the device appears undamaged in the standard STEM imaging channels (Figs. 5a–

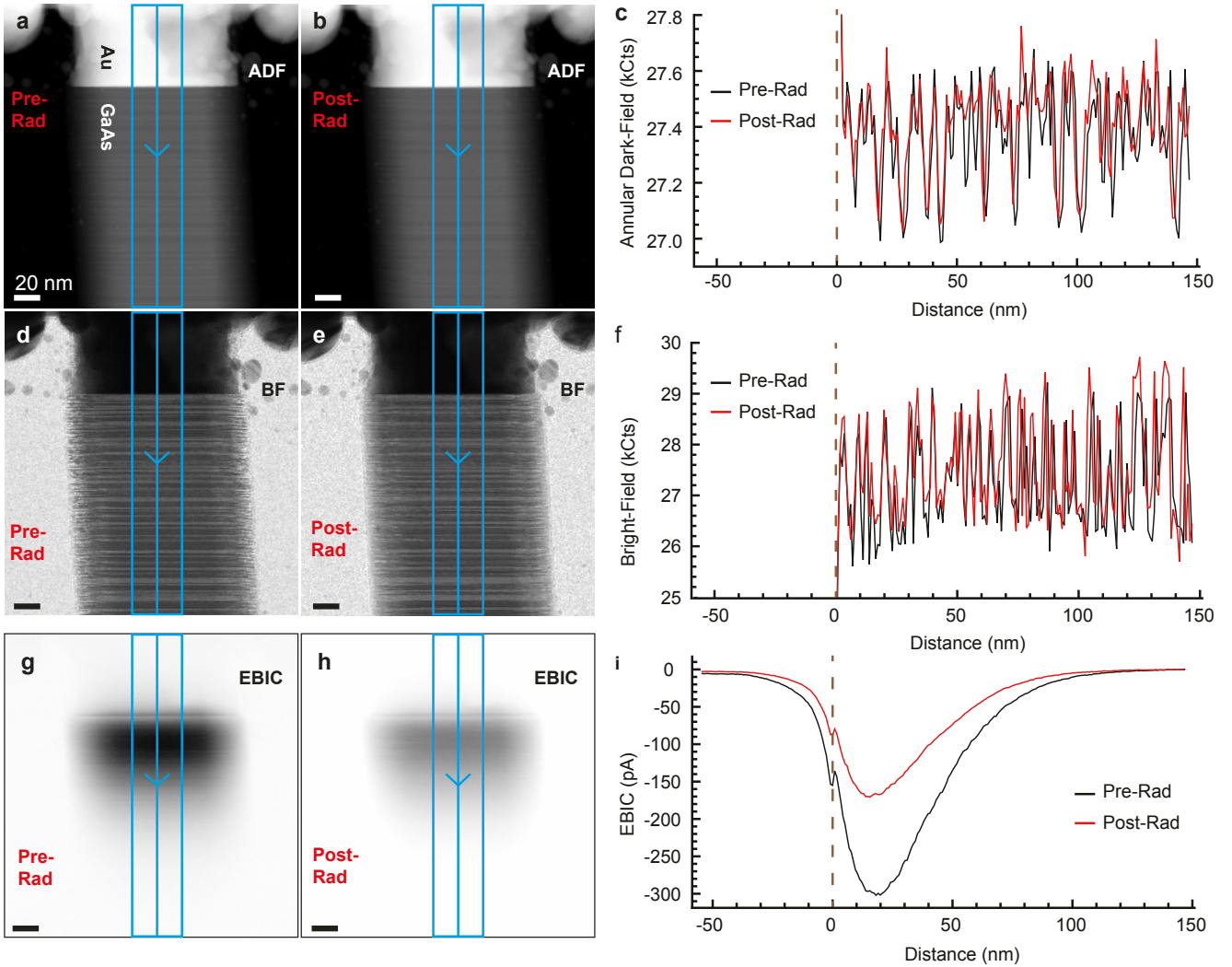


FIG. 5. Annular dark-field, bright-field, and EBIC imaging before and after irradiation with 300 kV STEM electrons. STEM ADF, bright-field (BF), and STEM EBIC images acquired before (a,d,g) and after (b,e,h) a dose of 6.0×10^6 e^-/nm^2 at 300 kV accelerating voltage. The total dose is applied while acquiring the twelve images #22–#33 (Fig. 4) and three alignment images (between #21 and #22). Line profiles are extracted (c,f,i) by horizontally averaging data within the blue boxes. A dashed brown line in the line profiles indicates the Au-GaAs interface. Irradiation produces almost no change in the conventional imaging channels (ADF, BF), but a 44% decrease in the maximum EBIC, which highlights the advantage of EBIC over conventional imaging for revealing functional properties such as the CCE.

f). But while standard STEM imaging is blind to the inserted defects, which have a relatively minor effect on the nanowire's physical structure, EBIC imaging (Figs. 5g–i), vividly reveals their outsize impact on the nanowire's electronic structure (namely a 44% reduction of the maximum EBIC).

The device of Figs. 2–5 is part of a larger circuit (Fig. 6). At low magnification a second heterojunction, on an adjacent nanowire but also in the circuit, is visible. The second heterojunction is imaged at lower magnification and less frequently (4.8 nm pixel size, 0.762 μs dwell time), and is thus subjected to less than 1% of the radiation dose of the irradiated junction. This adjacent

junction can control for changes that are independent of radiation dose.

To corroborate the role of radiation-induced defects in the observed EBIC reduction, after image #33 of Figs. 4–5 we anneal the nanowire device in an inert argon atmosphere at 250°C for 30 minutes. Such treatment reduces the density of VI defects within the nanowire, since the elevated temperature makes the beam-induced defects mobile, allowing interstitials and vacancies to meet and annihilate[40, 44]. After the annealing treatment, we image the nanowire heterojunction again (Fig. 6). The anneal restores the EBIC to its pre-irradiated value (i.e. restores the 44% lost) while changing the measured

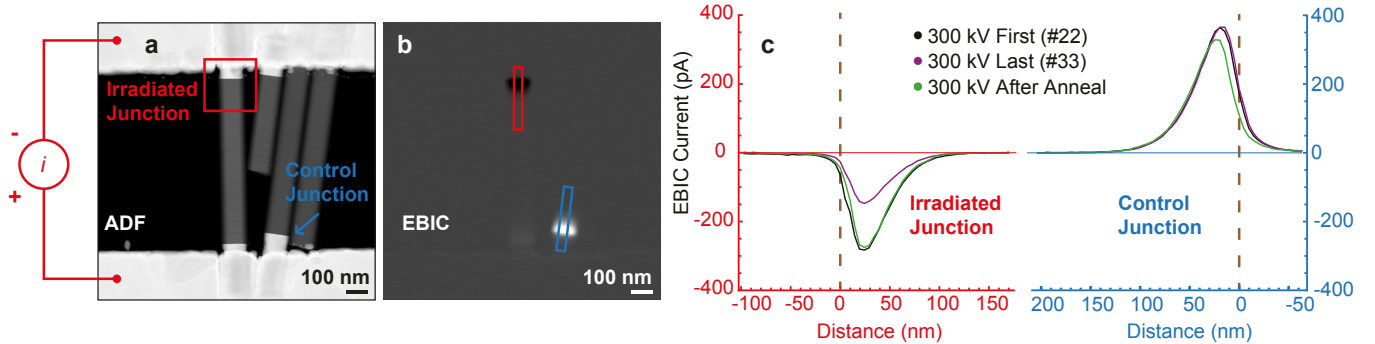


FIG. 6. **STEM EBIC before and after annealing.** A low-magnification STEM ADF image (a) of the device of Figs. 2–5 shows both the heavily irradiated Au-GaAs heterojunction (red square) and the adjacent control, a heterojunction irradiated less frequently and only at low magnification (cyan arrow). The simultaneously-acquired EBIC image (b) shows that the two heterojunctions have EBICs with opposite signs because of their relative orientations in the circuit. The red and cyan rectangles in (b) indicate the sources of the line profiles in the red and cyan plots of (c). After irradiation with 300 kV electrons the magnitude of the irradiated heterojunction's EBIC is reduced relative to the control. After an anneal the irradiated heterojunction's EBIC recovers.

1 EBIC in the control junction by only a small amount 38
 2 ($< 10\%$). The post-anneal restoration is consistent with 39
 3 the hypothesis that the radiation-induced CCE reduction 40
 4 is caused by defects — specifically VI defects — that an- 41
 5 neal away at high temperature. 42

6 The STEM's precise electron beam positioning allows 43
 7 us to observe the effect of selectively dosing just part of 44
 8 the nanowire. In an experiment performed on the Fig. 6 45
 9 device (after the annealing experiment), we irradiate a 46
 10 narrow strip of GaAs that only spans half of the nanowire 47
 11 heterojunction (denoted by dashed green box in Fig. 7a). 48
 12 With 300 kV, a 50 pA beam current, a 0.633 nm pixel 49
 13 size, and a 2.3 ms pixel dwell time, the dose per area per 50
 14 strip image, $1.8 \times 10^6 \text{ e}^-/\text{nm}^2$, is $5.5 \times$ that of the Fig. 4 51
 15 experiment. As in the experiment of Fig. 6, we acquire 52
 16 low dose images before and after the high-dose images 53
 17 for purposes of comparison. (Here a 153 μs dwell time 54
 18 and 1.27 nm pixel size of the two low-dose images con- 55
 19 tributes only 1.1% of the combined dose from the three 56
 20 strip images.) The difference between the before and 57
 21 after images (Fig. 7d) shows that the localized strip irra- 58
 22 diation decreases the CCE across the entire width of the 59
 23 nanowire. 60

24 By comparing consecutive EBIC images we can, in 61
 25 some cases, precisely identify the position where an 62
 26 electrically-active defect is inserted. ADF (Fig. 7 e1, e2, 63
 27 e3) and EBIC (f1, f2, d3) images are collected simultane- 64
 28 ously in the three high-dose strip images. In the (stan- 65
 29 dard) raster pattern used here, the electron beam scans 66
 30 across one row from left to right, and then moves down 67
 31 to scan the next rows in sequence in the same direction. 68
 32 Each strip image shows a dose-induced EBIC decrease, 69
 33 as in Fig. 4. EBIC difference images (Fig. 7 g1, g2) reveal 70
 34 a sudden drop (8 pA magnitude) in the EBIC that occurs 71
 35 in a single 0.63 nm pixel. We attribute this sudden drop 72
 36 to the insertion of an electrically-active defect during the 73
 37 second strip image, at the pixel indicated by the yellow 74

cross (Fig. 7 e2). Notably, since the displaced atom of a VI defect can travel only a few angstroms from its original position at these low energies, and likely in the direction of the electron beam, the yellow cross marks the final location of this single defect [1, 42]. Thus the defect generation volume is much smaller than the e-h generation volume, and EBIC imaging is able to locate VI insertion events with a much higher precision ($< 1 \text{ nm}$) than its electronic resolution of $\approx 10 \text{ nm}$.

Comparing in Fig. 7g1 the 30 pixels to the left and to the right of the insertion event, and the four rows on either side, we find a pre-event EBIC difference of 7 pA and a post-event EBIC difference of 20 pA, with pixel-to-pixel standard deviations of 2.4 pA (Fig. S7). The $\sim 10\%$, single-pixel reduction in the EBIC is thus statistically significant, and it implies that the inserted defect's recombination cross-section σ is $\sim 10\%$ of the nanowire's 10^4 nm^2 physical cross section, i.e. $\sigma \simeq 10^{-11} \text{ cm}^2$. This cross section, while large, is within the range of those seen previously [45]. Electron irradiation specifically has been seen to introduce recombination centers with cross sections of this magnitude [46, 47].

As with all of the other STEM-beam induced radiation damage here, this insertion leaves no signature in the conventional ADF imaging. The CCE reduction from this individual defect insertion event is again non-local (as in Fig. 7d), since the difference between the first and third strip images (Fig. 7g3) is uniform.

In summary, STEM EBIC imaging with an electron-beam acceleration potential of 80 or 200 kV maps the CCE of a GaAs nanowire diode without damaging the device. The minority-carrier diffusion length is found to decrease significantly near the thin edges of the nanowire, and is thus limited by surface recombination. Imaging with the acceleration potential increased to 300 kV introduces defects in the nanowire that decrease the diode's CCE. These VI defects can be annealed away to restore

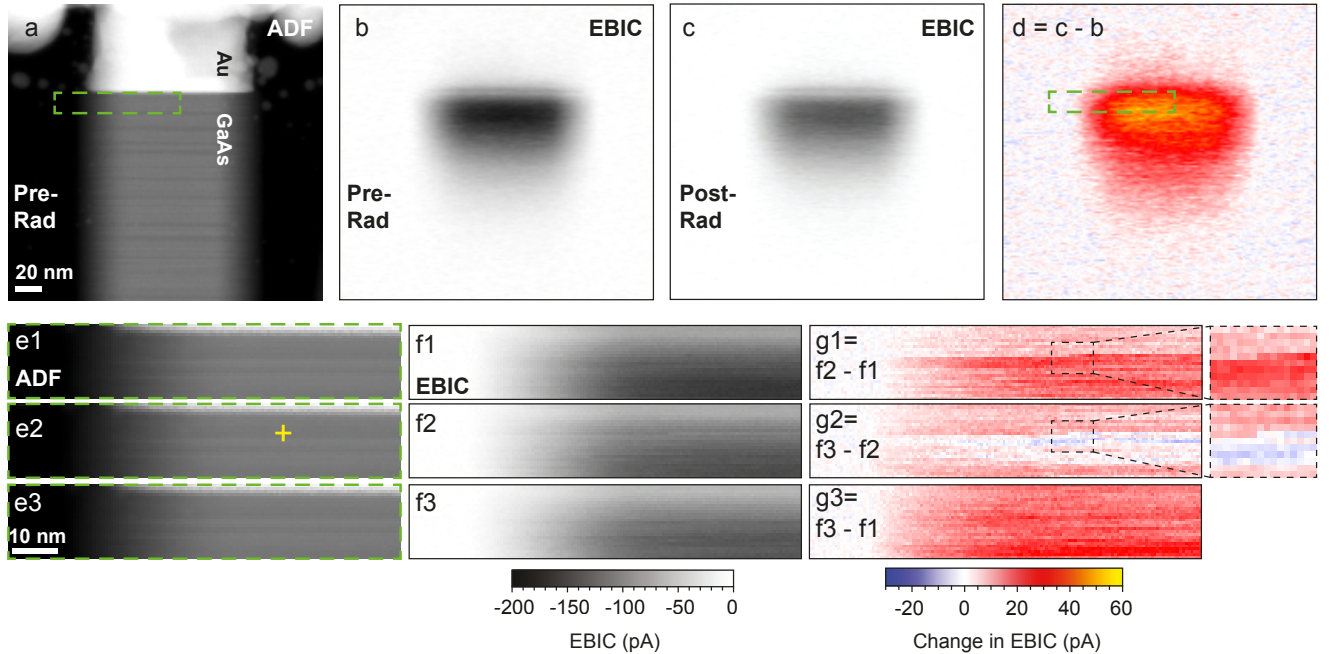


FIG. 7. Defect insertion and pinpoint localization with STEM EBIC at 300 kV. We record the initial state of an Au-GaAs nanowire heterojunction with low-dose ($3.0 \times 10^4 \text{ e}^-/\text{nm}^2$) ADF STEM (a) and STEM EBIC (b) images acquired simultaneously. We then image the region outlined by the dashed box (a) three times (e1,e2,e3) with a high dose ($1.8 \times 10^6 \text{ e}^-/\text{nm}^2$ per image). After the three strip images we acquire a second low-dose EBIC image (c). A difference image (d) shows that the EBIC decreases across the entire nanowire, even though the dose was confined to a narrow region on the left side of the nanowire. Dark-field strip images (e1,e2,e3) show no change during irradiation, while the simultaneously-acquired EBIC strip images (f1,f2,f3) show significantly smaller signals. EBIC difference images (g1, g2) reveal a sudden drop in the EBIC magnitude within one 0.63 nm pixel, indicating that a defect was inserted during the second strip image at the location indicated by the yellow cross (e2). Zoom regions (dashed boxes on g1, g2) of $11 \text{ pixels} \times 16 \text{ pixels}$ ($7 \text{ nm} \times 10 \text{ nm}$) demonstrate that both the row and the column of the insertion event can be located precisely. A difference image between the first and third strip image (g3) indicates that, as in (d), the electronic impact of the defect is delocalized. The black-white color scale applies to panels (b,c,f), and the blue-yellow color scale applies to panels d and g.

1 the original CCE of the diode. Despite being invisible 23 in conventional STEM imaging channels, a VI defect in- 24 serted at 300 kV can be precisely located by identifying 25 an abrupt drop in CCE as the electron beam rasters. 26 As these results show, a modern, variable-energy STEM 27 equipped for EBIC imaging is an experimentally potent 28 combination for producing, locating, and characterizing 29 defects in semiconductor devices with high spatial reso- 30 lution.

10 **Methods:** GaAs nanowires are grown by selective- 32 area epitaxy in a vertical metalorganic chemical vapor 33 deposition (MOCVD) reactor (Emcore D-75) at 60 Torr, 34 using hydrogen as a carrier gas. Triethylgallium (TEGa), 35 tertiarybutylarsine (TBAs), and diethylzinc (DEZn) are 36 used as precursors for gallium, arsenic, and zinc p-type 37 dopant, respectively. See supplementary information 38 for complete growth parameters. The GaAs nanowires' 39 measured resistivity is $\lesssim 5 \Omega\cdot\text{cm}$ (see Fig. S5 and re- 40 lated text), which in bulk GaAs corresponds to a dopant 41 concentration[48] of $\gtrsim 5 \times 10^{15} \text{ cm}^{-3}$.

21 Nanowires are mechanically transferred using a sharp 43 tungsten probe to 15 nm-thick silicon nitride windows re- 44

inforced with a $0.8 \mu\text{m}$ -thick backing layer of silicon oxide (Fig. S2). Nanowires are located with a scanning electron microscope (SEM), and individual electron-beam lithography patterns are written to each silicon nitride window using polymethylmethacrylate (PMMA) resist. The samples are dipped in 1:10 hydrofluoric acid:water solution for 60 seconds to remove native GaAs oxides. Immediately afterward, samples are placed in an electron-beam evaporation chamber and 250 nm of gold is deposited. Intruded gold contacts are formed by heating the samples in a rapid thermal annealer (RTA) at 340°C for 30 seconds in a nitrogen atmosphere. To make the sample electron-transparent, the silicon oxide support film is removed with a hydrofluoric acid vapor etch. The sample is loaded into a Hummingbird Scientific biasing holder with electrical feedthroughs. STEM images are acquired at 80, 200, and 300 kV accelerating voltage within an FEI Titan STEM. EBIC signal is measured using a FEMTO DLPICA-200 transimpedance amplifier, set to $10^9 \Omega$ gain with 40 kHz bandwidth. The amplified current signal is fed into an analog input in the STEM, and is synced to the STEM probe position to form an EBIC image.

Acknowledgments: This work was supported by National Science Foundation (NSF) awards DMR-1611036 and DMR-2004897, NSF STC award DMR-1548924 (STROBE), and Sêr Cymru grants in Advanced Engineering. Data were collected at the Electron Imag-

ing Center for Nanomachines (EICN) at the California NanoSystems Institute (CNSI). Samples were fabricated in the Integrated Systems Nanofabrication Cleanroom (ISNC) at the CNSI. We thank Ting-Yuan Chang for assistance with patterning the nanowire growth template.

[1] Allan Johnston, *Reliability and Radiation Effects in Compound Semiconductors* (World Scientific, Singapore, 2010).

[2] Matthew D. McCluskey and Eugene E. Haller, *Dopants and Defects in Semiconductors*, second edition. ed. (CRC Press, Taylor & Francis Group, Boca Raton, FL, 2018).

[3] Ellen Hieckmann, Markus Nacke, Matthias Allardt, Yury Bodrov, Paul Chekhonin, Werner Skrotzki, and Jörg Weber, “Comprehensive Characterization of Extended Defects in Semiconductor Materials by a Scanning Electron Microscope,” *JoVE (Journal of Visualized Experiments)*, e53872 (2016).

[4] J. R. Srour and J. W. Palko, “Displacement Damage Effects in Irradiated Semiconductor Devices,” *IEEE Transactions on Nuclear Science* **60**, 1740–1766 (2013).

[5] Fajun Li, Ziyuan Li, Liying Tan, Yanping Zhou, Jing Ma, Mykhaylo Lysevych, Lan Fu, Hark Hoe Tan, and Chen-nupati Jagadish, “Radiation effects on GaAs/AlGaAs core/shell ensemble nanowires and nanowire infrared photodetectors,” *Nanotechnology* **28**, 125702 (2017).

[6] L. C. Hirst, M. K. Yakes, J. H. Warner, M. F. Bennett, K. J. Schmieder, R. J. Walters, and P. P. Jenkins, “Intrinsic radiation tolerance of ultra-thin GaAs solar cells,” *Applied Physics Letters* **109**, 033908 (2016).

[7] C. O. Thomas, D. Kahng, and R. C. Manz, “Impurity Distribution in Epitaxial Silicon Films,” *Journal of The Electrochemical Society* **109**, 1055–1061 (1962).

[8] D. V. Lang, “Deep-level transient spectroscopy: A new method to characterize traps in semiconductors,” *Journal of Applied Physics* **45**, 3023–3032 (1974).

[9] K. C. Collins, A. M. Armstrong, A. A. Allerman, G. Vizkelethy, S. B. Van Deusen, F. Léonard, and A. A. Talin, “Proton irradiation effects on minority carrier diffusion length and defect introduction in homoepitaxial and heteroepitaxial n-GaN,” *Journal of Applied Physics* **122**, 235705 (2017), publisher: American Institute of Physics.

[10] Jeffrey H. Warner, Scott R. Messenger, Robert J. Walters, Geoffrey P. Summers, Manuel J. Romero, and Edward A. Burke, “Displacement Damage Evolution in GaAs Following Electron, Proton and Silicon Ion Irradiation,” *IEEE Transactions on Nuclear Science* **54**, 1961–1968 (2007), conference Name: IEEE Transactions on Nuclear Science.

[11] Volker Naumann, Dominik Lausch, Angelika Hähnel, Jan Bauer, Otwin Breitenstein, Andreas Graff, Martina Werner, Sina Swatek, Stephan Großer, Jörg Bagdahn, and Christian Hagendorf, “Explanation of potential-induced degradation of the shunting type by Na decoration of stacking faults in Si solar cells,” *Solar Energy Materials and Solar Cells* **120**, 383–389 (2014).

[12] Brian D. Hoskins, Gina C. Adam, Evgheni Strelcov, Nikolai Zhitenev, Andrei Kolmakov, Dmitri B. Strukov, and Jabez J. McClelland, “Stateful characterization of resistive switching TiO₂ with electron beam induced currents,” *Nature Communications* **8**, 1972 (2017), number: 1 Publisher: Nature Publishing Group.

[13] D. Ban, E. H. Sargent, St. J. Dixon-Warren, I. Calder, A. J. SpringThorpe, R. Dworschak, G. Este, and J. K. White, “Direct imaging of the depletion region of an InP p–n junction under bias using scanning voltage microscopy,” *Applied Physics Letters* **81**, 5057–5059 (2002).

[14] Christoph Gutsche, Raphael Niepelt, Martin Gnauck, Andrey Lysov, Werner Prost, Carsten Ronning, and Franz-Josef Tegude, “Direct Determination of Minority Carrier Diffusion Lengths at Axial GaAs Nanowire p–n Junctions,” *Nano Letters* **12**, 1453–1458 (2012).

[15] Chia-Chi Chang, Chun-Yung Chi, Maoqing Yao, Ningfeng Huang, Chun-Chung Chen, Jesse Theiss, Adam W. Bushmaker, Stephen LaLumondiere, Ting-Wei Yeh, Michelle L. Povinelli, Chongwu Zhou, P. Daniel Dapkus, and Stephen B. Cronin, “Electrical and Optical Characterization of Surface Passivation in GaAs Nanowires,” *Nano Letters* **12**, 4484–4489 (2012).

[16] Jonathan E. Allen, Eric R. Hemesath, Daniel E. Perea, Jessica L. Lensch-Falk, Z. Y. Li, Feng Yin, Mhairi H. Gass, Peng Wang, Andrew L. Bleloch, Richard E. Palmer, and Lincoln J. Lauhon, “High-resolution detection of Au catalyst atoms in Si nanowires,” *Nature Nanotechnology* **3**, 168–173 (2008).

[17] C. Donolato, “Contrast and resolution of SEM charge-collection images of dislocations: Applied Physics Letters: Vol 34, No 1,” *Appl. Phys. Lett.* **34**, 80–81 (1979).

[18] Ludwig Reimer, *Scanning Electron Microscopy: Physics of Image Formation and Microanalysis*, 2nd ed., Springer Series in Optical Sciences ; v. 45 (Springer, Berlin, 1998).

[19] M. Kociak and L. F. Zagonel, “Cathodoluminescence in the scanning transmission electron microscope,” *Ultramicroscopy* 70th Birthday of Robert Sinclair and 65th Birthday of Nestor J. Zaluzec PICO 2017 – Fourth Conference on Frontiers of Aberration Corrected Electron Microscopy, **176**, 112–131 (2017).

[20] E. R. White, Alexander Kerelsky, William A. Hubbard, Rohan Dhall, Stephen B. Cronin, Matthew Mecklenburg, and B. C. Regan, “Imaging interfacial electrical transport in graphene–MoS₂ heterostructures with electron-beam-induced-currents,” *Applied Physics Letters* **107**, 223104 (2015).

[21] Jonathan D. Poplawsky, Chen Li, Naba R. Paudel, Wei Guo, Yanfa Yan, and Stephen J. Pennycook, “Nanoscale doping profiles within CdTe grain boundaries and at the CdS/CdTe interface revealed by atom probe tomography and STEM EBIC,” *Solar Energy Materials and Solar Cells* **150**, 95–101 (2016).

[22] Myung-Geun Han, Matthew S. J. Marshall, Lijun Wu, Marvin A. Schofield, Toshihiro Aoki, Ray Tweten, Jason Hoffman, Frederick J. Walker, Charles H. Ahn, and Yimei Zhu, “Interface-induced nonswitchable domains in

1 ferroelectric thin films," *Nature Communications* **5**, 4693 57
 2 (2014). 58

3 [23] Zoey Warecki, Vladimir Oleshko, Kimberlee Celio, An- 59
 4 drew Armstrong, Andrew Allerman, A. Alec Talin, and 60
 5 John Cumings, "Measuring the minority carrier diffusion 61
 6 length in n-GaN using bulk STEM EBIC," *Microscopy* 62
 7 and *Microanalysis* **24**, 1842–1843 (2018). 63

8 [24] William A. Hubbard, Matthew Mecklenburg, Ho Leung 64
 9 Chan, and B. C. Regan, "STEM Imaging with Beam- 65
 10 Induced Hole and Secondary Electron Currents," *Physi- 66
 11 cal Review Applied* **10**, 044066 (2018). 67

12 [25] Matthew Mecklenburg, William A. Hubbard, Jared J. 68
 13 Lodico, and B. C. Regan, "Electron beam-induced cur- 69
 14 rent imaging with two-angstrom resolution," *Ultrami- 70
 15 croscopy* **207**, 112852 (2019). 71

16 [26] Aidan P. Conlan, Grigore Moldovan, Lucas Bruas, Eva 72
 17 Monroy, and David Cooper, "Electron beam induced 73
 18 current microscopy of silicon p–n junctions in a scan- 74
 19 ning transmission electron microscope," *Journal of Ap- 75
 20 plied Physics* **129**, 135701 (2021). 76

21 [27] Hannah J. Joyce, Jennifer Wong-Leung, Qiang Gao, 77
 22 H. Hoe Tan, and Chennupati Jagadish, "Phase Perfec- 78
 23 tion in Zinc Blende and Wurtzite III-V Nanowires Using 79
 24 Basic Growth Parameters," *Nano Letters* **10**, 908–915 80
 25 (2010). 81

26 [28] Kimberly A. Dick, Claes Thelander, Lars Samuelson, 82
 27 and Philippe Caroff, "Crystal Phase Engineering in Sin- 83
 28 gle InAs Nanowires," *Nano Letters* **10**, 3494–3499 (2010). 84

29 [29] Daniel Rudolph, Stefan Funk, Markus Döblinger, Ste- 85
 30 fanie Morkötter, Simon Hertenberger, Lucas Schweick- 86
 31 ert, Jonathan Becker, Sonja Matich, Max Bichler, Danëe 87
 32 Spirkoska, Ilaria Zardo, Jonathan J. Finley, Gerhard 88
 33 Abstreiter, and Gregor Koblmüller, "Spontaneous Al- 89
 34 loy Composition Ordering in GaAs-AlGaAs Core–Shell 90
 35 Nanowires," *Nano Letters* **13**, 1522–1527 (2013). 91

36 [30] Marta Orrù, Silvia Rubini, and Stefano Roddaro, "For- 92
 37 mation of axial metal–semiconductor junctions in GaAs 93
 38 nanowires by thermal annealing," *Semiconductor Science 94
 39 and Technology* **29**, 054001 (2014). 95

40 [31] Vidar T. Fauske, Junghwan Huh, Giorgio Divitini, 96
 41 Dasa L. Dheeraj, A. Mazid Munshi, Caterina Ducati, 97
 42 Helge Weman, Bjørn-Ove Fimland, and Antonius T. J. 98
 43 van Helvoort, "In Situ Heat-Induced Replacement of 99
 44 GaAs Nanowires by Au," *Nano Letters* **16**, 3051–3057¹⁰⁰
 45 (2016). 101

46 [32] Melanie Nichterwitz and Thomas Unold, "Numerical¹⁰²
 47 simulation of cross section electron-beam induced current¹⁰³
 48 in thin-film solar-cells for low and high injection condi-¹⁰⁴
 49 tions," *Journal of Applied Physics* **114**, 134504 (2013). 105

50 [33] Vitor R. Manfrinato, Jianguo Wen, Lihua Zhang, Yujia¹⁰⁶
 51 Yang, Richard G. Hobbs, Bowen Baker, Dong Su, Dmitri¹⁰⁷
 52 Zakharov, Nestor J. Zaluzec, Dean J. Miller, Eric A.¹⁰⁸
 53 Stach, and Karl K. Berggren, "Determining the Resolu-¹⁰⁹
 54 tion Limits of Electron-Beam Lithography: Direct Mea-¹¹⁰
 55 surement of the Point-Spread Function," *Nano Letters*¹¹¹
 56 **14**, 4406–4412 (2014).

[34] Brian Zutter, *Imaging Electrically-Active Defects in Gal- 57
 58 lium Arsenide and Cobalt Nanowire Devices*, Ph.D. the-
 sis, UCLA (2021).

[35] Jacob B. Khurgin, "Fundamental limits of hot carrier 59
 60 injection from metal in nanoplasmonics," *Nanophotonics* 61
 62 **9**, 453–471 (2020).

[36] Pierre Hovington, Dominique Drouin, and Raynald Gau- 63
 64 vin, "CASINO: A new Monte Carlo code in C language 65
 66 for electron beam interaction —part I: Description of the 67
 68 program," *Scanning* **19**, 1–14 (1997).

[37] Dominique Drouin, Alexandre Réal Couture, Dany Joly, 69
 70 Xavier Tastet, Vincent Aimez, and Raynald Gauvin, 71
 72 "CASINO V2.42—A Fast and Easy-to-use Modeling Tool 73
 74 for Scanning Electron Microscopy and Microanalysis 75
 76 Users," *Scanning* **29**, 92–101 (2007).

[38] A. Rothwarf, "Plasmon theory of electron-hole pair pro- 77
 78 duction: efficiency of cathode ray phosphors," *Journal of 79
 80 Applied Physics* **44**, 752–756 (1973).

[39] R.F. Egerton, *Electron Energy-Loss Spectroscopy in the 81
 82 Electron Microscope*, 3rd ed. (Springer, 2011).

[40] A. Pillukat, K. Karsten, and P. Ehrhart, "Point defects 83
 84 and their reactions in e-irradiated GaAs investigated by 85
 86 x-ray-diffraction methods," *Physical Review B* **53**, 7823– 87
 88 7835 (1996).

[41] K. Nordlund, J. Peltola, J. Nord, J. Keinonen, and 89
 90 R. S. Averback, "Defect clustering during ion irradiation 91
 92 of GaAs: Insight from molecular dynamics simulations," 93
 94 *Journal of Applied Physics* **90**, 1710–1717 (2001).

[42] Nanjun Chen, Sean Gray, Efrain Hernandez-Rivera, Dan- 95
 96 hong Huang, Paul D. LeVan, and Fei Gao, "Compu- 97
 98 tational simulation of threshold displacement energies 99
 100 of GaAs," *Journal of Materials Research* **32**, 1555–1562 101
 (2017).

[43] R. F. Egerton, R. McLeod, F. Wang, and M. Malac, 102
 103 "Basic questions related to electron-induced sputtering 104
 105 in the TEM," *Ultramicroscopy Proceedings of the Inter- 106
 107 national Workshop on Enhanced Data Generated by 108
 109 Electrons*, **110**, 991–997 (2010).

[44] L. W. Aukerman and R. D. Graft, "Annealing of 109
 110 Electron-Irradiated GaAs," *Physical Review* **127**, 1576– 111
 1583 (1962).

[45] J. C. Bourgoin, H. J. von Bardeleben, and D. Stiévenard, 112
 113 "Native defects in gallium arsenide," *Journal of Applied 114
 115 Physics* **64**, R65–R92 (1988).

[46] G.M. Martin, A. Mitonneau, and A. Mircea, "Electron 116
 117 traps in bulk and epitaxial GaAs crystals," *Electronics 118
 119 Letters* **13**, 191 (1977).

[47] D. V. Lang and L. C. Kimerling, "A new technique for 119
 120 defect spectroscopy in semiconductors: Application to 1- 121
 122 Mev electron irradiated n-GaAs," in *Lattice Defects in 123
 124 Semiconductors*, Institute of Physics Conference Series 125
 126 No. 23 (Institute of Physics, London, 1974) pp. 581–588.

[48] S. M. Sze and J. C. Irvin, "Resistivity, mobility and im- 127
 128 purity levels in GaAs, Ge, and Si at 300k," *Solid-State 129
 130 Electronics* **11**, 599–602 (1968).